PERGAMON

International Journal of Heat and Mass Transfer 45 (2002) 2739–2753

International Journal of HEAT and MASS TRANSFER

www.elsevier.com/locate/ijhmt

Heat induced transition of a stable vortex street

R.N. Kieft, C.C.M. Rindt *, A.A. van Steenhoven

Faculty of Mechanical Engineering, Eindhoven University of Technology, WH-3.129, P.O. Box 513, Eindhoven 5600 MB, The Netherlands

Received 10 January 2001; received in revised form 8 August 2001

Abstract

A combined numerical and experimental investigation is presented showing the effect of heat on the stability of a horizontal vortex street for $Re_D = 75$ and Ri_D between 1 and 2. Detailed 2D-HiRes PV experiments are compared with 2D numerical results. The results show that an early transition to 3D of the vortex street takes place for $Ri_D > 1$. Furthermore, the location at which the 2D wake becomes essentially 3D turns out to be dependent on Ri_D. For an increasing addition of heat (increasing Ri_D), this location is shifted into the direction of the cylinder. By applying 3D measuring techniques, such as 3D-PTV and 3D visualisation techniques, the transition process and the behaviour downstream of the transition point are investigated.

Keywords: Cylinder; Transitional; Wakes

1. Introduction and problem definition

The stability of wake flows is of interest for several reasons. From a fundamental point of view the prediction of the transition from a 2D to a 3D state was and still is a big issue for many researchers. Besides, from a more practical point of view also a strong interest exists in the (in)stability of wake flows. Considering for example heat exchange equipment, a transition of the wake inherently means an increase of exchange rate between the wake flow and its surrounding environment. Consequently, heat dissipating components positioned in this wake will probably experience an increased cooling efficiency.

The stability of the wake is strongly dependent on the Reynolds number (Re_D). For moderate Reynolds numbers ($Re_D < 150$) and no heat addition, the shed vortex structures form a strongly linked pattern or vortex street. This vortex street turns out to be very stable. For $50 < Re_D < 100$ it even remains stable and 2D until the vortices are fully dissipated [1]. For higher Reynolds numbers ($Re > 150$), several investigations show that the vortex street starts to transit, triggered by spanwise disturbances. Depending on Re_D these disturbances result in an α or β mode instability [2].

For $50 < Re_D < 150$ a vortex street transition can be exhilarated by external sources, for example, by adding a vibration to the cylinder. For frequencies close to the natural vortex shedding frequency and for sufficiently large amplitudes, the vortex structures become deformed. This can eventually lead to an early breakdown of the vortex street [3–5].

Also addition of heat will have an effect on the vortex street stability. Considering the upward flow around a heated cylinder, it turns out that heat stabilises the vortex street characteristics [6–8]. First a slight increase in the vortex shedding frequency can be observed but a further increase of heat addition results in the formation of two steady twin vortices. For a horizontal vortex street behind a heated cylinder it is found that addition of heat results in a disturbed vortex street eventually giving rise to an early transition [9].

The present investigation focuses on the early transition of the horizontal vortex street due to the addition of heat. The problem to be investigated (Fig. 1(a)) consists of a horizontal heated cylinder with constant temperature T_1 which is exposed to a uniform horizontal

* Corresponding author Tel.: +31-40-247-2978; fax: +31-40-243-3445.

E-mail address: c.c.m.rindt@tue.nl (C.C.M. Rindt).

0017-9310/02/$ - see front matter
PII: S0017-9310(01)00356-8

Nomenclature

D	cylinder diameter (m)
f	vortex shedding frequency (s^{-1})
f	frame number
g	gravity acceleration (m/s^2)
$\vec{g}$	gravity vector (dimensionless)
Gr_D	Grashof number ($= (\beta g(T_1 - T_0)D^3)/\nu^2$)
L	length cylinder (m)
p	pressure (dimensionless)
Pr	Prandtl number ($= \nu/\alpha$)
Re_D	Reynolds number ($= U_0 D/\nu$)
Ri_D	Richardson number ($= Gr_D/Re_D^2$)
t	time (s) or dimensionless time
T	period time (s)
T_1	cylinder wall temperature (K)
T_0	free stream temperature (K)
$\vec{u}$	velocity vector (dimensionless)
U_0	free stream velocity (m/s)
x	x-position in test section (m)
x_c	x-position of the cylinder (m)
y	y-position in test section (m)

Greek symbols

α	thermal diffusivity
β	cubic expansion coefficient
ν	kinematic viscosity
$\vec{\omega}$	the vorticity vector (dimensionless)
ω_z	third component of the vorticity vector (dimensionless)
Θ	temperature difference [$= (T - T_0)/(T_1 - T_0)$, dimensionless]

cold cross-flow with velocity U_0 (≈1 cm/s) and temperature T_0 (≈20 °C). The cylinder has an outer diameter D (= 8.5 mm) and a length L (= 495 mm), resulting in an aspect ratio equal to $L/D \approx 60$. The main flow is directed perpendicular to the gravity vector. The appearance of an induced buoyant force will result in a violation of the symmetry. The considered flow can be described by the dimensionless Boussinesq equation

$$\nabla \cdot \vec{u} = 0, \tag{1}$$

$$\frac{\partial \vec{u}}{\partial t} + \vec{u} \cdot \nabla \vec{u} = -\nabla p + \frac{1}{Re_D} \nabla^2 \vec{u} - Ri_D \Theta \vec{g}, \tag{2}$$

$$\frac{\partial \Theta}{\partial t} + \vec{u} \cdot \nabla \Theta = \frac{1}{Re_D Pr} \nabla^2 \Theta, \tag{3}$$

with $Re_D = U_0 D/\nu$ the Reynolds number, $Ri_D = g\beta \Delta T D/U_0^2$ the Richardson number, $Pr = \nu/\alpha$ the Prandtl number and α the thermal diffusivity, ν the kinematic viscosity, g the gravity constant and β the thermal expansion coefficient. For the Richardson numbers under consideration, the temperature differences ΔT ($= T_1 - T_0$) are in the range of $0 < \Delta T < 5$ °C.

From the momentum equation, the vorticity equation can be derived:

$$\frac{\partial \vec{\omega}}{\partial t} + \vec{u} \cdot \nabla \vec{\omega} - (\vec{\omega} \cdot \nabla)\vec{u} = Ri_D \frac{\partial \Theta}{\partial x} + \frac{1}{Re_D} \nabla^2 \vec{\omega}, \tag{4}$$

with $\vec{\omega}$ the vorticity vector. For a 2D flow the vorticity vector $\vec{\omega}$ reduces to a vector with only an out-of-plane component ω_z. The vorticity equation can then be written as a kind of scalar transport equation

$$\frac{\partial \omega_z}{\partial t} + \vec{u} \cdot \nabla \omega_z = Ri_D \frac{\partial \Theta}{\partial x} + \frac{1}{Re_D} \nabla^2 \omega_z, \tag{5}$$

where ω_z is the out-of-plane component of the vorticity vector $\vec{\omega}$, which is defined as

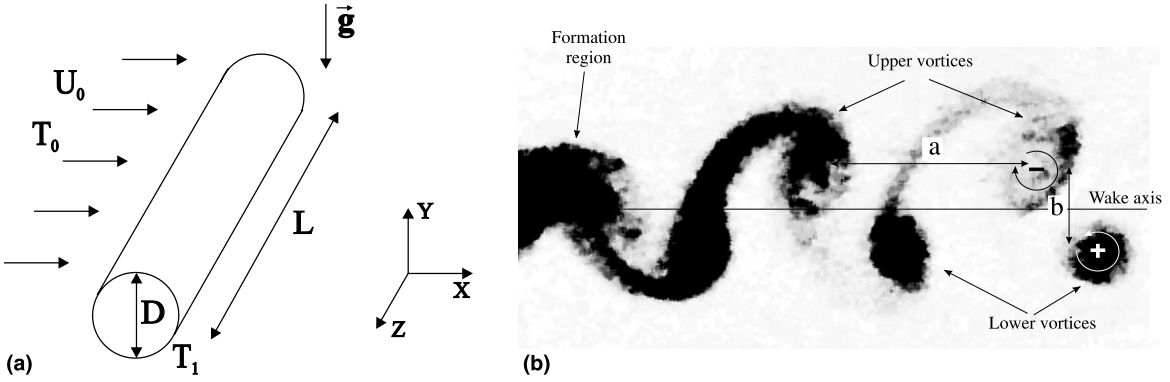

Fig. 1. Problem definition: (a) configuration and (b) typical flow field example.

$$\omega_z = \frac{\partial v}{\partial x} - \frac{\partial u}{\partial y}. \quad (6)$$

Comparing the 2D vorticity equation with a general scalar transport equation it can be seen that the first term on the right-hand side represents a source term. This source term is referred to as the baroclinic production term. It represents a production of vorticity within the flow domain due to temperature gradients perpendicular to the gravity vector. With respect to an isothermal flow, heat addition will cause the total circulation (integrated vorticity over the entire domain) to change.

As one can see, the relative importance of the heat induced effects is indicated by the Richardson number. Within the present investigation Ri_D will vary between 1 and 2. For $0 < Ri_D < 1$ the wake characteristics do change [10] but the global character of the vortex street remains 2D. A typical example of such a flow is shown in Fig. 1(b). In this figure the staggered pattern of vortex structures is clearly visible. The pattern exists out of upper and lower vortices. For larger heat addition ($Ri_D > 1$) it is to be expected that heat induced processes, as vorticity production, will influence the stability of the vortex street.

Here, the influence of the heat induced processes and the mechanism involved in the early transition to 3D of the vortex street will be addressed. To that end, experiments are performed. For these experiments a towing tank is designed in which visualisation techniques and 2D and 3D particle tracking techniques are used. The background information of these experiments is presented in Section 2. To study the onset to transition also 2D simulations are accomplished. The numerical technique used will be briefly explained in Section 3. Comparison of the 2D experimental and numerical results gives insight into the phenomena responsible for the transition, as shown in Section 4. Results of the 3D investigation are presented in Section 5. The article ends up with a brief discussion and some concluding remarks.

2. Experimental methods

The experiments are performed in a water tank [11] in which the flow is created by towing the cylinder through the relatively motionless fluid. The cylinder is positioned within the water tank by clamping it between two glass plates, connected to a translation system. Advantages of such a towing tank are small boundary layers and well-preserved inflow conditions. The observed transitional phenomena are therefore fully generated by the heat induced effects. Another major advantage of a towing tank is that the construction allows to analyse the evolution of the shed vortex structures quite easily. Once shed from the cylinder, the vortex structures do almost not move with respect to the fixed world. Therefore the evolution of the structures can be analysed in detail over a relatively long period (about 6–8 typical shedding periods). Transitional processes which take place further downstream can thus easily be analysed.

2.1. Visualisation

Detailed qualitative information is obtained from fluorescent dye visualisations. The visualisation fluid is injected by a multiple-needle injection probe. This probe has eight needles spaced uniformly in the z-direction over a span of 7 cm. By injecting the fluid just ahead of the cylinder, streak-lines are created representing the flow field behaviour behind the cylinder. The injection velocity is chosen equal to the towing velocity ($\approx$10 mm/s), so only little disturbance of the main flow is expected. Viewing from above (Fig. 2(a)) the 3D effects manifest themselves by a disturbance of the original parallel streak-lines. In the visualisation also a second camera is used, viewing the experiments in spanwise direction (Fig. 2(b)).

2.2. 2D-high resolution particle velocimetry

For the 2D experiments a hybrid measurement technique between particle tracking velocimetry (PTV) and particle image velocimetry (PIV) is used. This results in a so-called high resolution particle velocimetry method (HiRes-PV) or super particle tracking. The algorithm functions according to the following steps. The captured images (image reader) are first filtered (dynamic thresholding). From the processed images the coordinates of the particles are determined (blob detection). The particle coordinates are re-mapped to a physical coordinate system. Particles in frame $f-1$ are then matched with a suitable candidate particle in frame f (matching). This matching algorithm is improved by using an estimation for the particle position in frame f. The estimated position is provided by a prediction algorithm. In case the previous matching result gives insufficient information for a prediction, external information from file can be retrieved for each frame on demand. For HiRes-PV the external information is obtained by executing a PIV algorithm on the acquired images. As a result, the flow field can be measured with about 7000–10 000 independent velocity vectors. This improves the spatial resolution with a factor 5 compared to more conservative techniques as PIV or PTV. Therefore the dynamics of the flow field can be captured with a high accuracy and high spatial resolution. More details about this technique can be found in [12].

2.3. 3D particle tracking velocimetry (3D-PTV)

The second method is a 3D extension of the particle tracking method. Instead of tracking particles in a

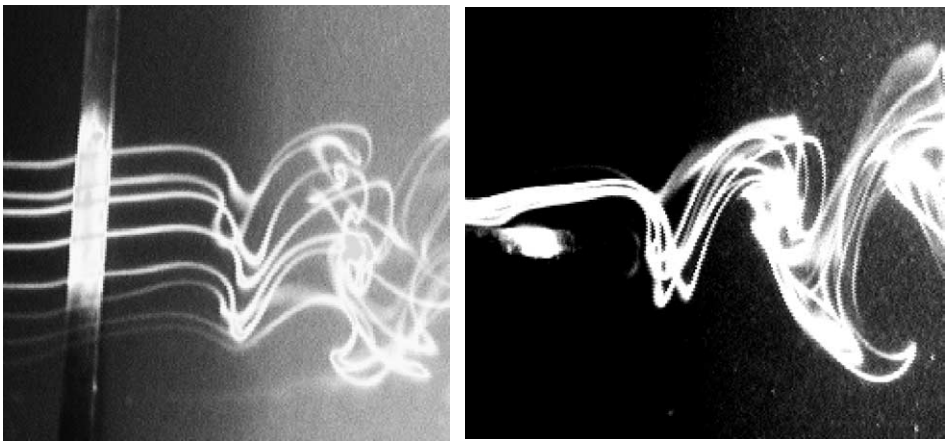

Fig. 2. Simultaneously acquired dye visualisation results of the vortex street: (a) viewed from above and (b) viewed along the cylinder axis.

thin light sheet, the particles are now tracked in an illuminated volume. In 3D-PTV methods at least two synchronised cameras need to be used. Only then stereo images can be obtained required to determine the 3D position of the particles (comparable to the human eye). By using only two cameras, the possibility exists that, especially for high seeding densities, particles are hiding behind each other. To decrease this effect of particle 'hide and seek' a third synchronised camera is applied which looks at the same volume as the other two cameras (Fig. 3(a)). A third camera also reduces the ambiguity occurring during the 3D localisation.

The 3D measuring method used within the present investigation is based on the above-described 2D particle tracking method. The main difference appears after the blob detection. Where as the 2D algorithm allows a direct start of the matching procedure, in the 3D-PTV routine the blobs detected in the three separate cameras need to be correlated (mapping lines of possible positions). Only then the three separate projections of a particle can be used to calculate its 3D position (3D localisation). Details about this localisation algorithm and its performance are described in [13].

3. Numerical method

Parallel to the experiments, 2D numerical simulations are performed. For an efficient temporal discretisation of the Boussinesq equations (Eqs. (2) and (3)), the (non-)linear convection–diffusion equations are split. This splitting operation is performed by applying a suitable integration factor [14]. As a result, a separate diffusion and convection equation remains which can be discretised separately. The convection equation is temporally discretised applying a three-step explicit Taylor–Galerkin scheme. The diffusion equation is discretised by an implicit second-order backwards difference scheme. The pressure term, which arises in the diffusion equation as a kind of source term, is treated by an approximate projection scheme [15].

For the spatial discretisation a high-order spectral element method (SEM) is used which can be considered as a mixture of a finite element method (FEM) [16] and a spectral method. The SEM combines the advantages of both latter mentioned methods. The principle is relatively straightforward. Within a small domain inside the fluid, a so-called element, the equations are discretised by using a spectral method. Combining the solutions obtained in all these elements results in the solution on the entire domain. Of course, special consideration has to be given to the continuity of the solution over the element boundaries. This decomposition of the domain in elements gives the method the geometric flexibility which can also be found in the FEM. By using a spectral approach within such an element a spectral convergence rate and small numerical errors, as numerical dispersion and diffusion, can be found.

4. Results

4.1. HiRes-PV results

The effect of heat addition on the transition from a 2D to a 3D flow is first analysed by performing 2D HiRes-PV experiments in the x–y plane. Reference to

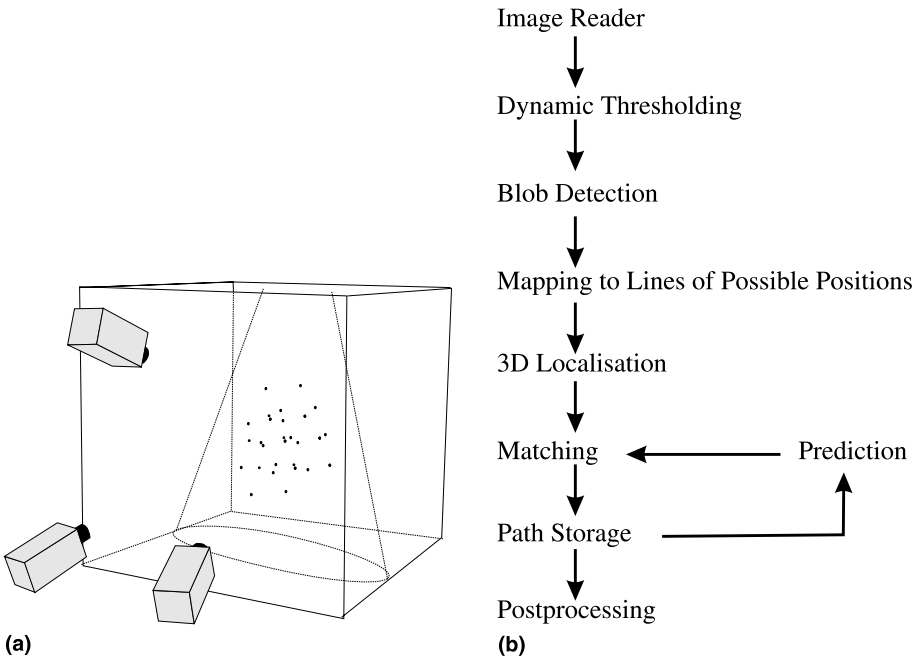

Fig. 3. 3D-PTV technique: (a) experimental set-up and (b) particle tracking algorithm.

the cylinder can be made using the cylinder position x_c/D, as indicated in the figures. The processes related to heat addition are here illustrated for $Re_D = 75$ and $Ri_D = 1.3$. For other Ri_D numbers within the range 1–2 similar phenomena were observed as illustrated later. On the left-hand side the velocity field at different locations behind the cylinder is presented (Fig. 4(a),(c),...,(i)). From these velocity fields the vorticity distribution is calculated (Fig. 4(b),(d),...,(j), contours between -1.6 and 1.6 with step size 0.1). Both the velocity and vorticity fields show clearly that just after the cylinder has passed the interrogation window (Fig. 4(a) and (b)) two stable coherent vortex structures are shed (situated at $x/D = 3$ and $x/D = 4.5$). These structures appear as the regular vortex structures which can also be observed in the 2D wake analysis [10]. A more detailed analysis of the structures reveals that some slight deformation of the structures takes place. These deformations cause the lower vortex to stretch in a positive y-direction while the upper vortex deforms into a horseshoe-shaped structure (Fig. 4(d)).

Near the negative upper vortex an area of positive vorticity is growing. This area grows further and moves in the positive y-direction (Fig. 4(d)). Simultaneously, the surrounding negative structure stretches and an upward moving vorticity strand is formed. At the tip of this strand, a local extreme can be observed (Fig. 4(f) at $x/D = 3.0$, $y/D = 3.0$) which becomes separated from the primary structure. This separated blob of negative vorticity forms a combined vortex structure with the further developed area of positive vorticity. This combined vortex structure which appears in the 2D slice as a dipole structure accelerates and leaves the interrogation area (Fig. 4(h) and (j)). An exact copy of this process can also be observed in the upper vortex positioned somewhat more downstream (around $x/D \approx 8.0$ in Fig. 4(b),(d),...,(j)).

Considering the evolution of the primary vortex structures, the vorticity contours show that after the dipole structure has escaped, the upper vortex seems to restore again but becomes significantly weaker. Also the lower vortex, which moves underneath the upper vortex, becomes weaker. As soon as this lower vortex has moved entirely underneath the upper vortex, it seems to disappear. Therefore in the last analysed stages only the upper vortices and the tail of the escaped vortex structure can be observed. In the vector plots the escaping secondary dipole structure appears as an outburst of fluid from the primary upper vortex structure (Fig. 4(c) at $x/D = 2$, $y/D = 2$). This upward motion, originating in the primary vortex, increases (Fig. 4(e)) and develops as an upward moving plume. At the top of the plume the development of a dipole-like structure can be observed (see Fig. 4(g)). As soon as the dipole has escaped, the upper vortex seems to restore again. This can be clearly seen in Fig. 4(i) in which the velocity vectors around $(x/D, y/D) = (2, 0.5)$ show a circulation area again. At the position of the lower vortex almost no circulation can be observed in the last two vector plots (Fig. 4(g) and (i)).

4.2. Numerical results

In order to analyse the development from a 2D to a 3D flow, the HiRes-PV results (showing the u, v components of the 3D velocity field) are compared with the results of 2D simulations. The simulations are performed for $Ri_D = 1.3$ and $Re_D = 75$. The development of the flow is analysed by a sequence of vorticity contours between $1 < t/\mathsf{T} < 2.5$ (iso-vorticity contours between -1.6 and 1.6 with step size 0.1). Again, the position of the cylinder x_c/D within the reference frame of the figures is presented.

Considering the vortex pair of which the upper vortex is positioned at $x/D = 2.5,\ y/D = 0.5$ and the lower

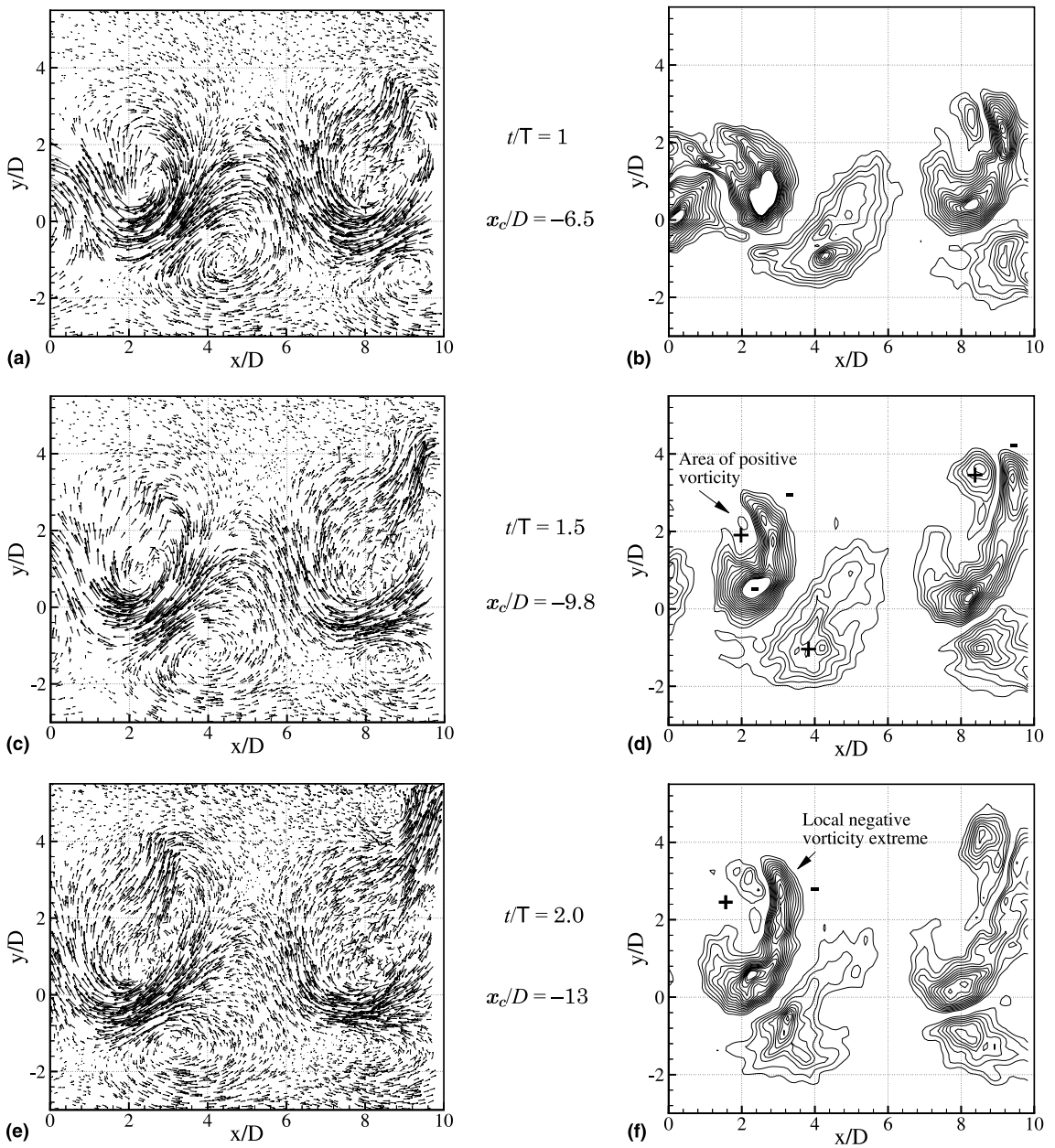

Fig. 4. Experimental results showing the development of the wake structures for $Re_D = 75$ and $Ri_D = 1.3$. Left: velocity field ($|U_0| \approx 1.05D$) and right: spanwise vorticity field (iso-vorticity contours $-1.6 < \omega_z < 1.6$ with step size 0.1). The position of the cylinder is denoted with x_c/D.

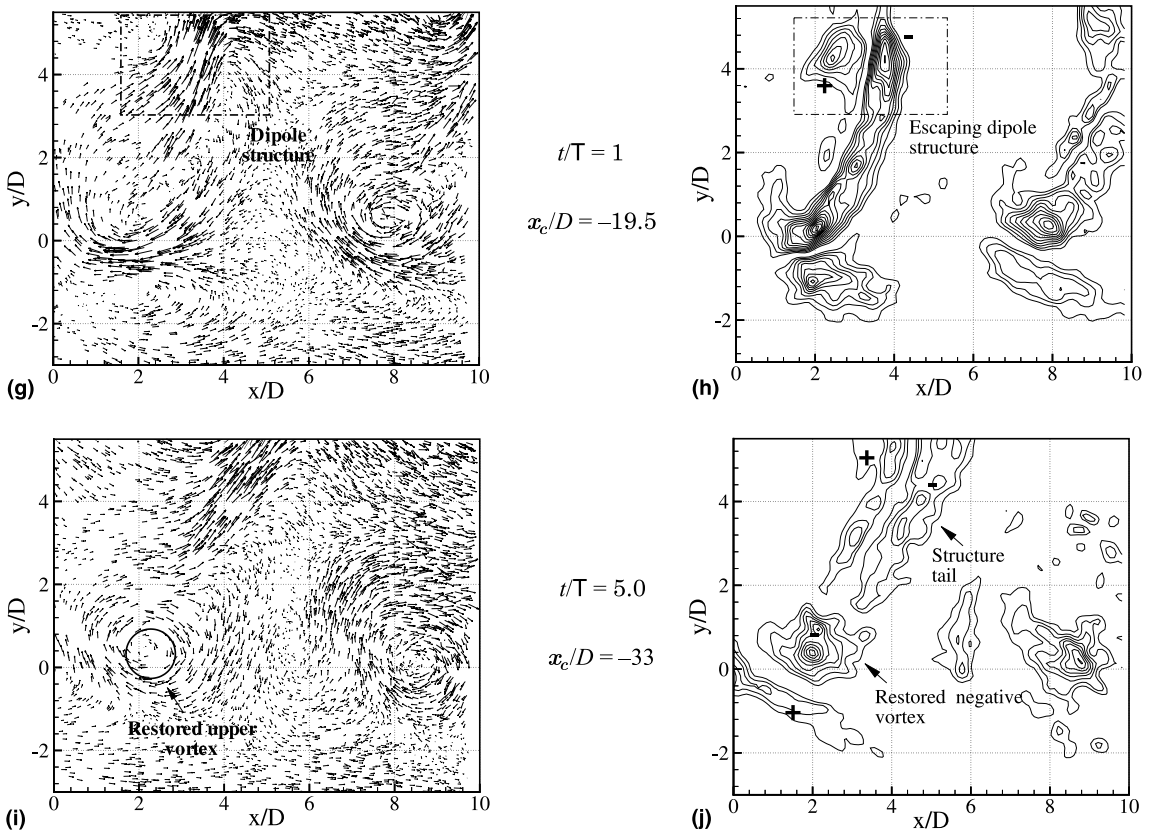

Fig. 4 (*continued*)

vortex at $x/D = 4$, $y/D = -1$, both the numerical and experimental results show a similar structure shape at $t/T \approx 1$ (Fig. 5(a) and (b)). Within the upper vortex a small disturbance can be observed which appears as an additional vorticity island causing the earlier observed structure deformation. Half a period later (Fig. 5(c) and (d)) this disturbance has developed further into a local area of positive vorticity inside a negative upper vortex.

For later stages, a difference appears between the experimental and the numerical results. In numerical results, the secondary structure continues to grow at a relatively fixed position within the surrounding primary upper vortex. This upper vortex shows the appearance of an upward stretched strand of negative vorticity (Fig. 5(f)). In the experimental results the secondary structure starts moving in the positive y-direction rather than growing inside the primary upper vortex (Fig. 5(e) and (g)). During this upward movement the secondary structure grows in size and strength. The deformation of the primary upper vortex, as observed in the numerical results, can also be seen in the experimental results. Only in these results, the upward stretching of a negative vorticity strand is observed to be stronger. The stretching is also extended to a higher y position and at the tip of the strand a local negative vorticity extreme appears (Fig. 5(e)). The formation of the dipole structure (Fig. 5(g)) and the escape of a secondary structure are processes which can only be observed in the experimental results. This allows to conclude that initially the development of the secondary structure is a 2D process, but that the escaping process (formation of a dipole structure and acceleration) is a 3D phenomenon.

Considering the lower vortex structure it is remarkable to see that during the entire analysed time span the experimentally and numerically determined structure behaviour is very similar. Therefore, it can be assumed that the lower vortex maintains, at least within the considered time span, its two-dimensional character.

From the comparison between the experimental and numerical results it was observed that the movement of the secondary structure in the positive y-direction could only be detected in the experimental results. The position where this upward movement starts will be denoted as the critical transition point x_{cr} in the transition to a 3D flow field. The localisation of this point is based on a qualitative analysis of the measured vorticity distribution. Therefore the accuracy of the determined location is limited and turns out to have a scatter of about

$\pm 1.5D$. Still, from the results a clear dependency of x_{cr} on Ri_D can be observed (Fig. 6). For decreasing Ri_D this critical point shows a tendency to move to a more downstream location. For $Ri_D < 1$ no escape of a secondary structure could be observed, at least not within the window of observation $0 < x/D < 35$. For increasing Ri_D this critical position seems to reach a limiting value, which is about $x/D = 10$–12.

From the numerical results also the temperature field and the baroclinic production of ω_z are analysed during the development of the secondary structure. The isothermals are plotted within the vorticity contours (dashed lines) for $0 < \Theta < 0.5$ using 21 levels (Fig. 7(a),(c),...,(i)). The iso-production contours are also plotted within the vorticity contours for $-0.5 < Ri_D \partial\Theta/\partial x < 0.5$ using 21 levels (Fig. 7(b),(d),...,(j)). The development of the secondary structure is analysed between $t/T = 1$ and $t/T = 3$. The plots of the temperature distribution show that heat is distributed within the flow field as isolated warm blobs (Fig. 7). These warm blobs are captured within the vortex structures and advected downstream without being influenced too much by mixing processes with their surroundings. Only heat diffusion processes can cause the extreme values to decrease. During the downstream convection the behaviour and deformation of the relatively warm blobs show a behaviour similar to that of the vortex structures. Also a strand, now containing warm fluid, is stretched in the positive y-direction (Fig. 7(e), (g) and (h)). This strand coincides with the stretched strand of negative vorticity. Relating this observation to the experimental results, it is expected that the experimentally observed vorticity strand, which is stronger and stretched more severely, contains a considerable amount of the heat originally contained by the primary structure. The escape of the secondary structure can possibly be seen as an effective way of releasing heat out of the primary structure.

The lower vortex structure seems to be hardly influenced by the induced heat. Only a slight increase of the structure temperature can be observed. The temperature of the lower structure appears to be about one order of magnitude smaller than the temperature of the upper vortex. As a result, the upper vortex is more affected by buoyancy than the lower vortex.

The presence of the temperature gradients in the horizontal direction gives rise to the baroclinic vorticity

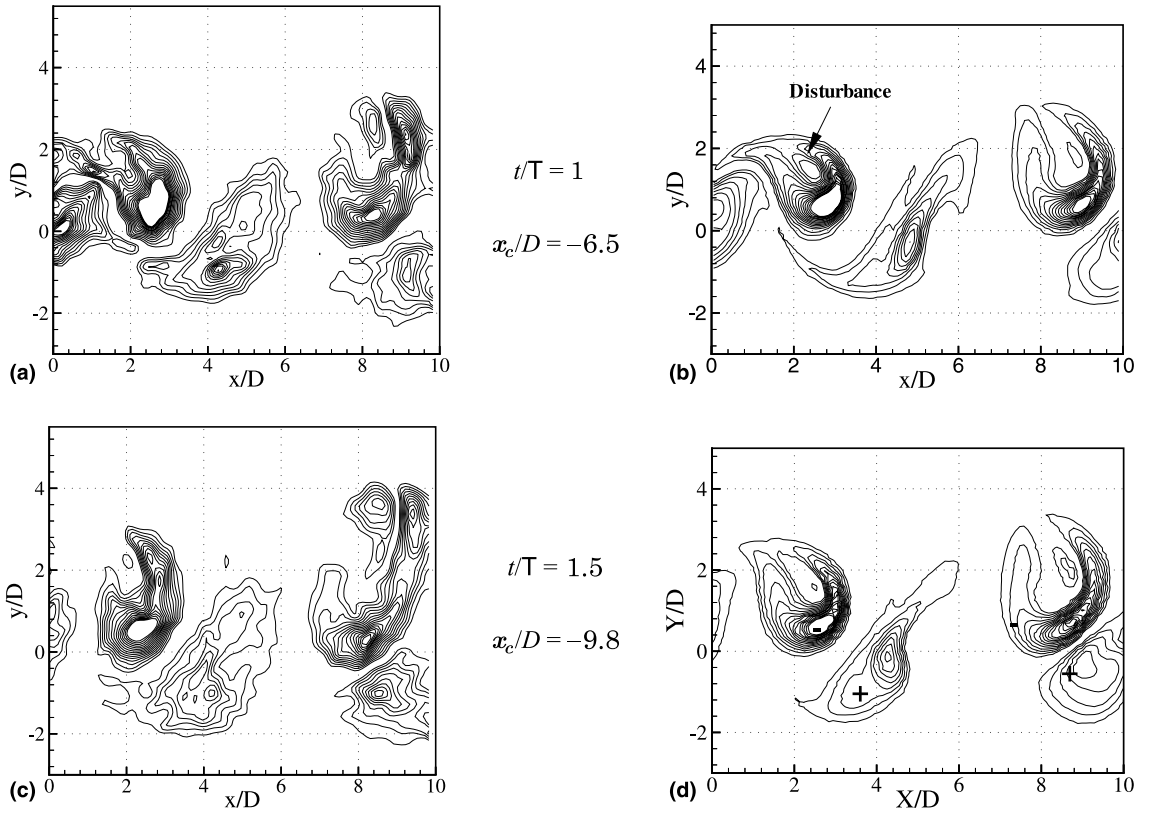

Fig. 5. Development of the spanwise vorticity distribution (iso-vorticity contours $-1.6 < \omega_z < 1.6$ with step size 0.1) for $Re_D = 75$ and $Ri_D = 1.3$. Left: experimental results and right: numerical results. The position of the cylinder is denoted with x_c/D.

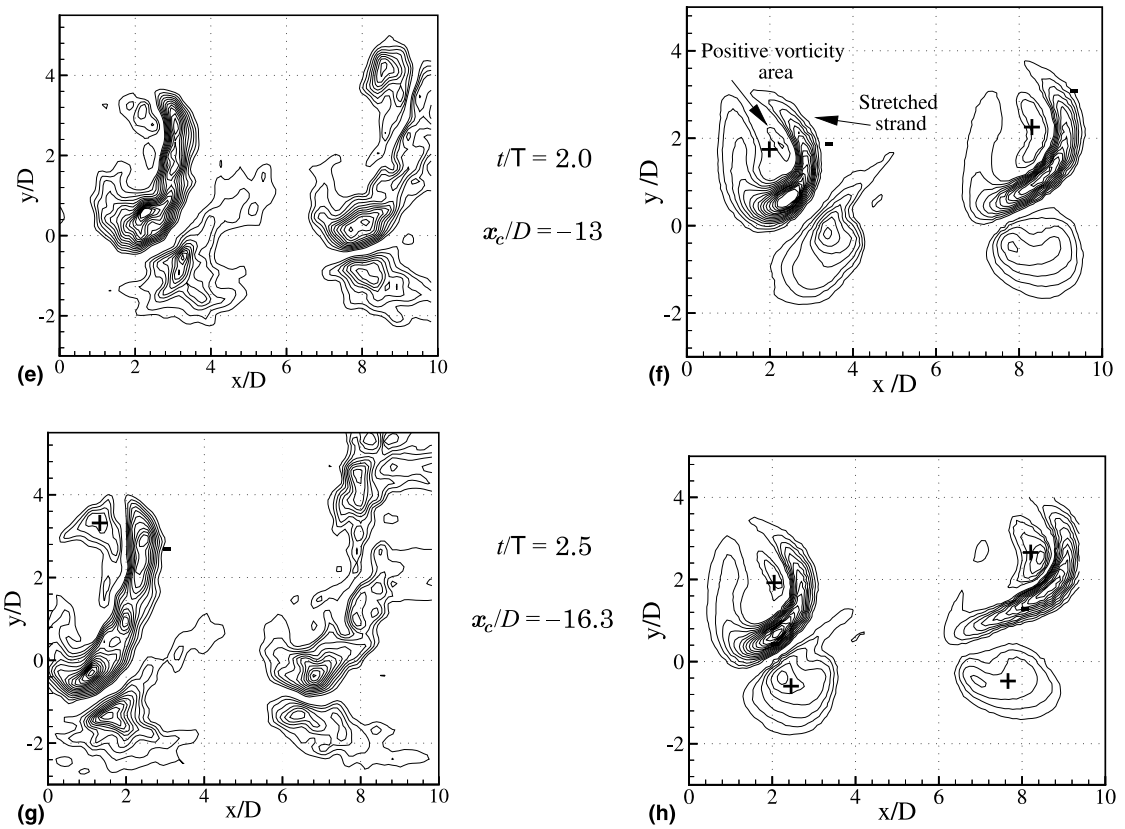

Fig. 5 (*continued*)

production (Fig. 7(b),(d),...,(h)). Inside an upper vortex structure a considerable area of positive and negative vorticity production can be found. A closer analysis reveals that the area of positive vorticity production coincides with the developing area of positive vorticity within the negative structure. This allows to conclude that the vorticity production is responsible for the development of the secondary structure. The area of negative production is found inside the primary upper vortex and stretched vorticity strand. This means that baroclinic vorticity production contributes to the strength of the vortex structure and adds to the stretching process of the negative strand. Considering the lower structure, almost no additional vorticity is produced within the structure. Only just after the formation, an area of negative and positive vorticity production can be observed which seems to be responsible for the deformation of the lower vortex structure (Fig. 7(b) and (d)).

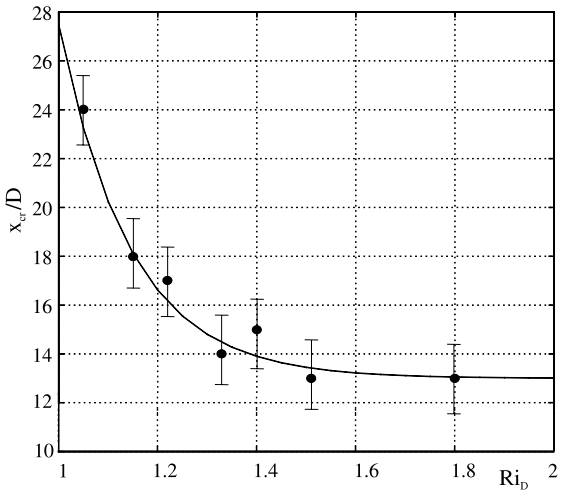

Fig. 6. Influence of Ri_D on x_{cr}.

4.3. 3D-results

4.3.1. Dye visualisations

The 3D behaviour of the vortex wake for $Ri_D > 1$ is further analysed by dye visualisations (Fig. 8). The dye streaks are recorded using two cameras. The first camera views the wake in spanwise direction (Fig. 8(a),

(c), ...,(k)) resulting in a side view of the wake flow. The cylinder is positioned at $(x/D, y/D) = (0, 0)$ and appears in the images as a slanted rectangle with a bright and a dark half. The images are captured every 2.5 s, which is almost equivalent to $2/5\mathsf{T}$, with T the typical shedding period ($\mathsf{T} = 6.5$ s).

Clearly visible in the sequence is the entrainment of injected dye from outside the upper shear layer into the cylinder near wake. Therefore, first the upper vortex becomes visible. More downstream dye is also advected into the lower vortex which becomes clearly observable for $x/D > 10$. More downstream the side view images show an additional dye blob on top of an upper vortex. This blob appears approximately at $x/D \approx 15$ (Fig. 8(a), denoted with the white arrow) and develops as it is convected downstream. At about $x/D \approx 20$ the dye blob escapes out of the primary upper vortex and develops into a mushroom-like shape. The mushroom shape is even better observable for a more downstream dye blob (called secondary structure and denoted with the white dashed arrow in Fig. 8(a),(c), ...,(k)). The upstream secondary structure (solid arrow) develops in a similar way and reaches the described stage at approximately the same downstream position (Fig. 8(k)).

The second camera views the flow from an oblique angle above (Fig. 8(b),(d), ...,(l)), thus providing information about spanwise variations. The images show that up to $x/D \approx 12$ the dye streak-lines remain almost parallel implying that no spanwise variations occur. In this region the flow is assumed to be 2D. More downstream, the development of the secondary structure takes place as indicated by the white dashed and solid arrows in Fig. 8(b)–(l). The secondary structure becomes apparent as the upward deflection of certain dye streaks. Therefore a spanwise variation in the streak-line behaviour can be observed, which indicates that the flow transforms into a 3D flow. However, the third velocity component seems to be small. This can be concluded from the dye streak-lines which show almost no deflections in the spanwise direction. Analysis of the recorded images has shown

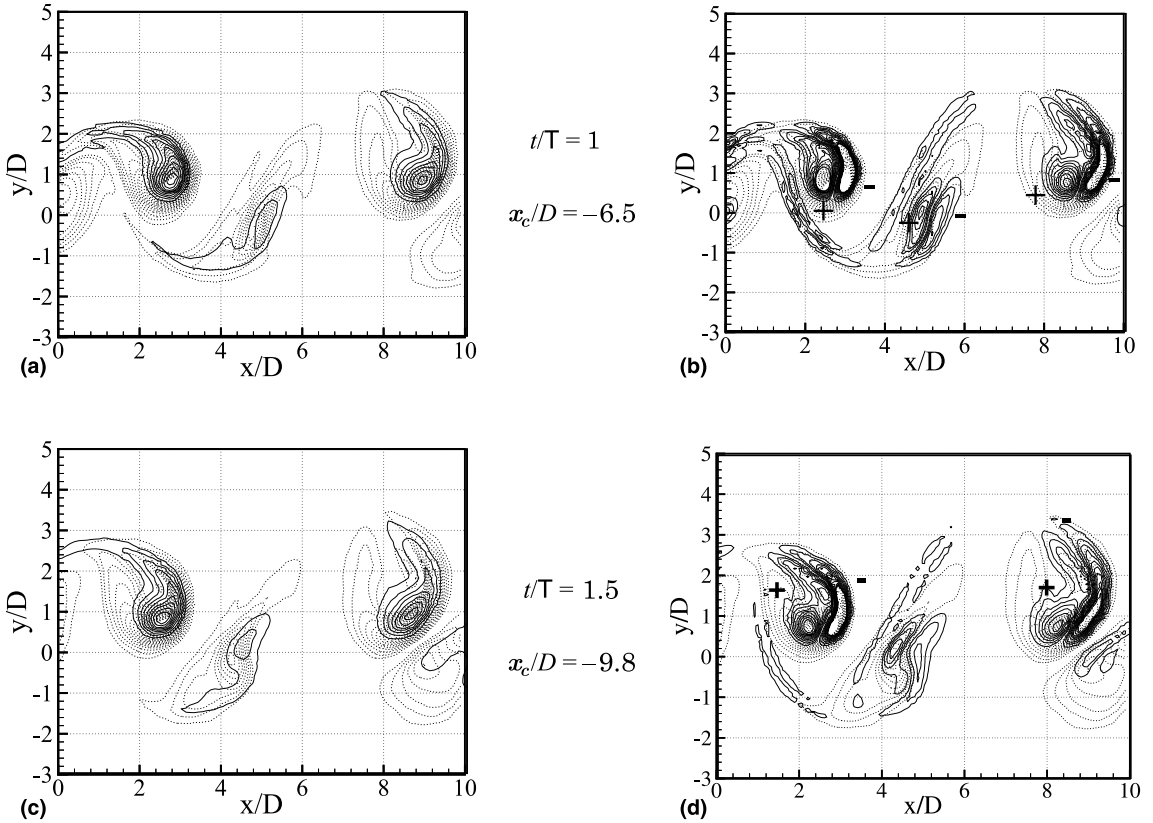

Fig. 7. Numerical results showing the development of the wake structures for $Re_D = 75$ and $Ri_D = 1.3$. Left: temperature field (solid lines: isothermals $0 < \theta < 0.5$ with step size 0.025) and right: baroclinic vorticity production (solid lines: $-0.5 < Ri_D \partial\theta/\partial x < 0.5$ with step size 0.05) within the spanwise vorticity distribution (dashed lines: $-1.6 < \omega_z < 1.6$ with step size 0.1). The position of the cylinder is denoted with x_c/D.

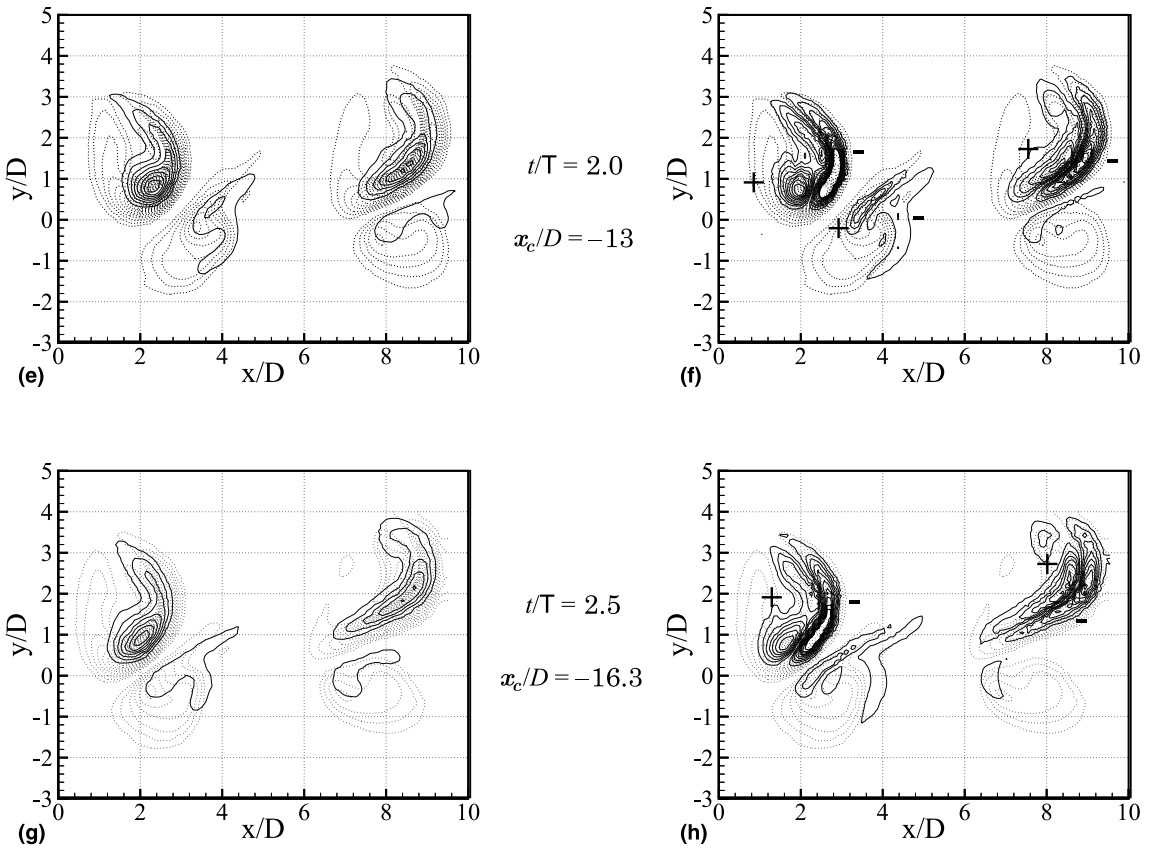

Fig. 7 (*continued*)

that at least at two spanwise positions a secondary structure develops. The spanwise distance between the two structures is estimated to be about 4D.

During the downstream convection, the escaping secondary structure develops into a vortex ring structure. This can be clearly seen from the escaping thermal structure as depicted by the dashed arrow in Fig. 8(f). In the planar view such a vortex ring is represented by a mushroom shape (Fig. 8(e)).

4.3.2. 3D-PTV

The 3D transition of the vortex wake flow and wake structures is investigated further by applying 3D-PTV experiments for $Ri_D > 1$. The experiments are performed with fixed camera positions, allowing to analyse in detail the evolution of the shed vortex structures to a 3D stage. The flow field is analysed in the domain $-5 < x/D < 5$, $-3 < y/D < 4$, $0 < z/D < 5$ and considering the previously presented visualisation and HiRes-PV experiments it is to be expected that within this domain a secondary escaping structure can be observed.

The 3D velocity fields are calculated from particles which could be tracked in five subsequent frames. Through these paths third-order functions are fitted from which the instantaneous velocity vectors can be derived. By doing so, in every frame about 400–500 velocity vectors are obtained. The noise in the velocity vectors is reduced by averaging the vector fields found over five subsequent samples. The averaging procedure is only allowed if the averaging period is considerably smaller than the typical time scale of the flow. This is indeed the case for the considered flow field where the typical flow period T is approximately 6.5 s and the averaging period is 0.2 s. From the averaged velocity field ω_z is calculated. The vorticity calculation is performed on a structured grid of $30 \times 30 \times 15$ elements. The unstructured velocity field is interpolated from the measured points (unstructured) to the grid using a 3D weighting interpolation [17].

The 3D wake transition process is analysed considering the spanwise component ω_z of the vorticity vector $\vec{\omega}$. As the 2D analysis has shown, this component shows the development of the secondary structure. The development is elucidated considering a negative and a positive iso-vorticity surface within the 3D domain, where the negative vorticity contour is presented by a shaded

surface and the positive vorticity by a meshed surface. In Fig. 9 the surfaces for $\omega_z = -0.25$ and $\omega_z = 0.15$ are presented. These surfaces represent clearly the primary upper and lower vortex structures and appear as 2D vortex tubes. Measuring noise possibly causes the observable spanwise variations. In a cross-section at $z/D = 1$ the primary upper and lower vortices can be clearly observed. The distribution is similar as the one observed in the 2D HiRes-PV results, although the latter results show much more details of the flow.

At $t/\mathrm{T} = 2$, the iso-surfaces of $\omega_z = -0.1$ and $\omega_z = 0.25$ show that around $(x/D, y/D, z/D) = (1, 2, 1)$ a patch of fluid is growing which contains positive vorticity (Fig. 9(c)). From the vorticity distribution at $z/D = 1$ it can be seen that this volume of positive vorticity is already linked with the negative vorticity of the primary structure resulting in the dipole-like secondary structure (Fig. 9(d)). This dipole structure then escapes from the primary upper vortex. This can be seen more clearly in the results at $t/\mathrm{T} = 2.7$ (Fig. 9(e) and (f)). Here a larger area of positive vorticity can be observed which forms a 3D linked structure with the strand of negative vorticity. The formed 3D-vortex ring structure escapes from the measuring domain. In the cross-section at $z/D = 1$ the vortex ring is observed as a dipole-like structure (Fig. 9(e)). The ω_z distribution in the cross-section shows a strong similarity with Fig. 5(f).

The 3D character of the flow becomes even more pronounced considering the cross-sections $z/D = 1$, $z/D = 2$ and $z/D = 4$ and $t/\mathrm{T} = 2.7$ (Fig. 10). The secondary structure is hardly visible at the cross-section at $z/D = 4$. Only a very small area of positive vorticity can be found at $(x/D, y/D) = (1, 2)$ and an upward stretched part of the upper vortex can be seen. In the cross-section at $z/D = 2$ the secondary structure can be observed already more clearly. Here a distinguished area of positive vorticity can be seen at $(x/D, y/D) = (1, 3)$ as well as a separate area of negative vorticity at $(x/D, y/D) = (2, 1)$. For $z/D = 1$ the secondary structure appears as a fully developed dipole structure.

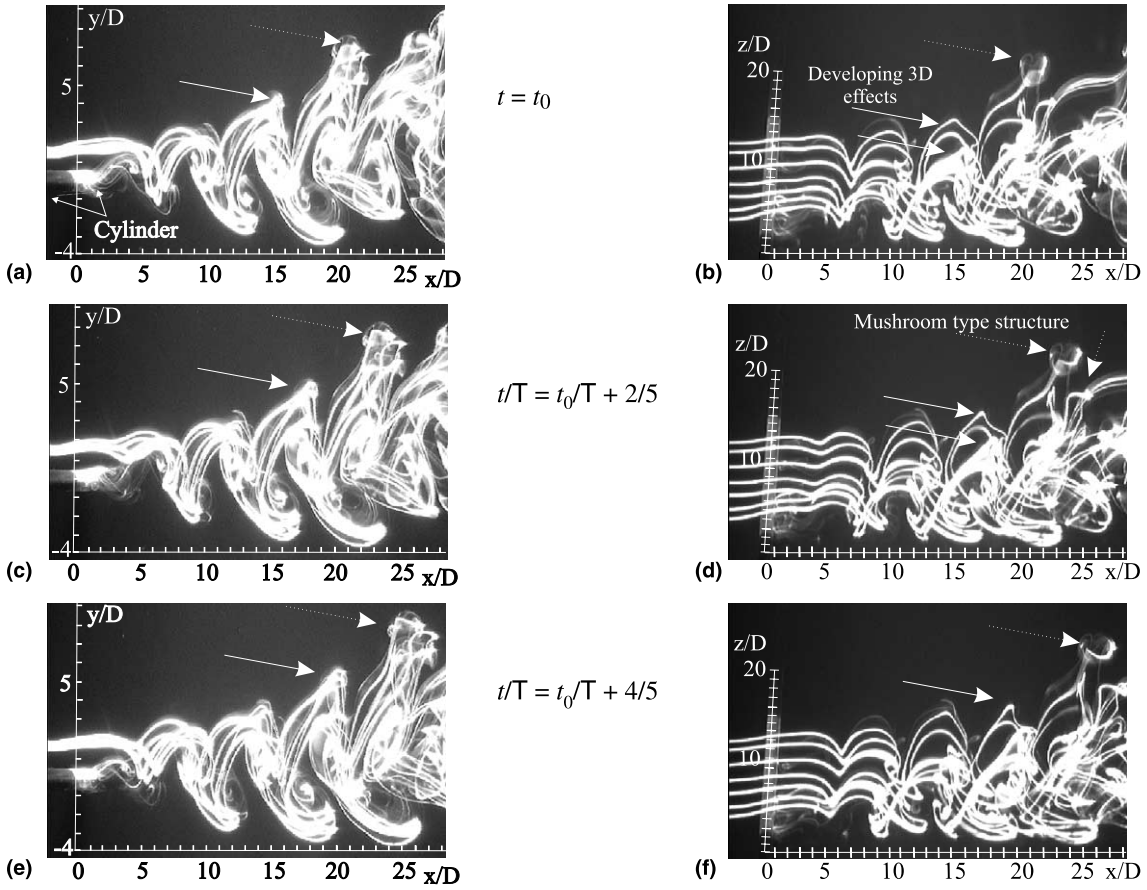

Fig. 8. Dye visualisations for $Re_D = 75$ and $Ri_D = 1.3$. Left: side view and right: oblique view. The dashed and solid arrows point in both sequences to the same structure. The cylinder is positioned in $x/D = 0$.

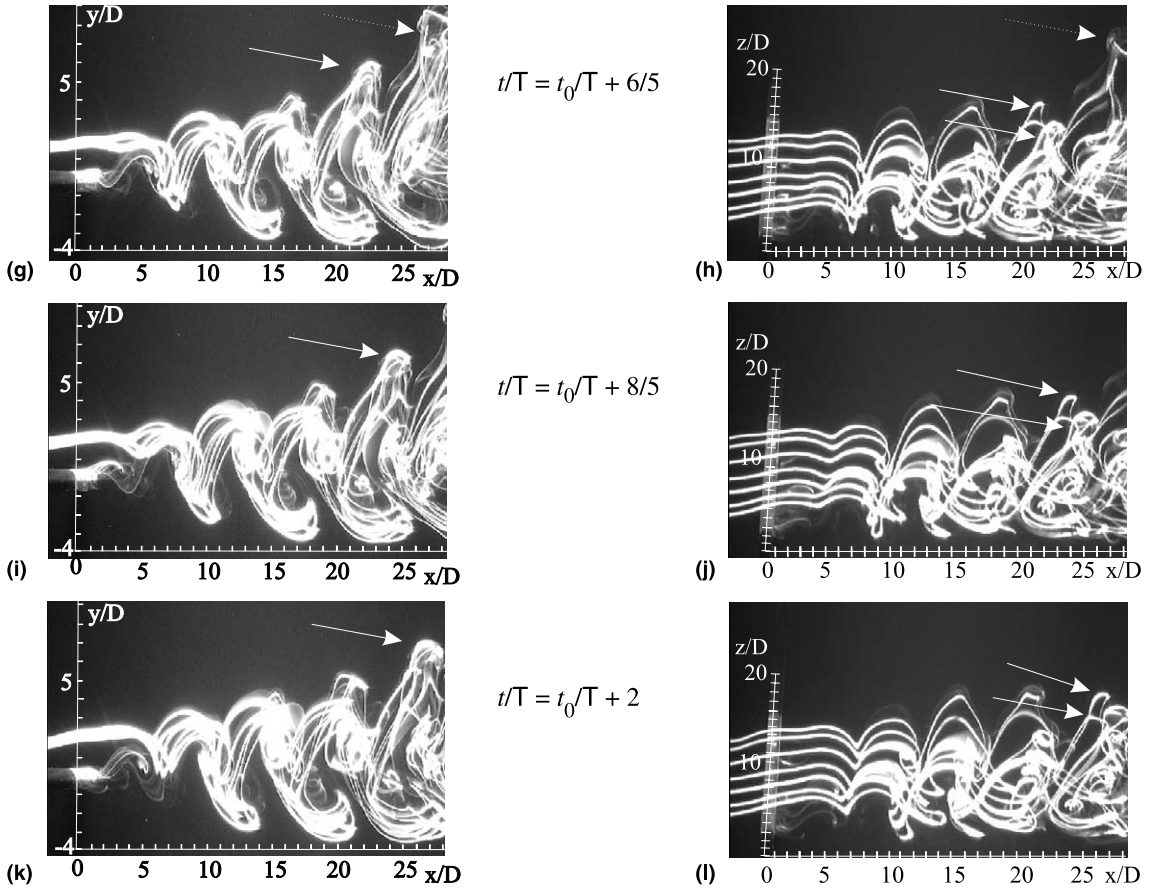

Fig. 8 (*continued*)

5. Discussion and conclusions

The results presented have shown that for $Ri_D > 1$ a 3D transition of the 2D vortex street is observed within the measurement area ($0 < x/D < 35$). The transition involves the following subsequent steps:

- Deformation of the upper vortex structure.
- Appearance of a local area of positive vorticity, generated by baroclinic vorticity production. This area can be found within the negative upper vortex.
- Formation of a dipole-like secondary structure consisting of the area of positive vorticity and a part of the negative upper vortex.
- Escape of the secondary vortex structure from the primary parental upper vortex.

In the first two steps the flow is observed to remain more or less 2D. Therefore these processes can also be observed in the 2D simulations. The formation of the dipole (which turns out to be a vortex-ring-like structure in 3D) and its escape (steps 3 and 4) is only observed in the experimental results. The 3D-PTV experiments as well as the 3D-dye visualisations have shown that these phenomena are 3D processes. Therefore, between step 2 and step 3 a transition to an essentially 3D flow occurs. Within the present investigation as a critical transition point the downstream position is taken at which the secondary structure starts to accelerate in positive y-direction. This critical point shows a rather strong dependency on Ri_D. Considering the lower vortices, the results have shown that these vortices remain 2D during the entire transition process.

Furthermore, the numerical simulations have shown that the upper vortices become more or less warm patches of fluid which are, due to their strong structure circulation, isolated from the surrounding environment. The lower vortices on the other hand seem to be hardly affected by heat. Therefore buoyancy has a more significant influence on the upper vortices than on the lower vortices.

The 3D visualisations show that the escape of a secondary structure takes place at distinguished spanwise positions. Although precise measurement results

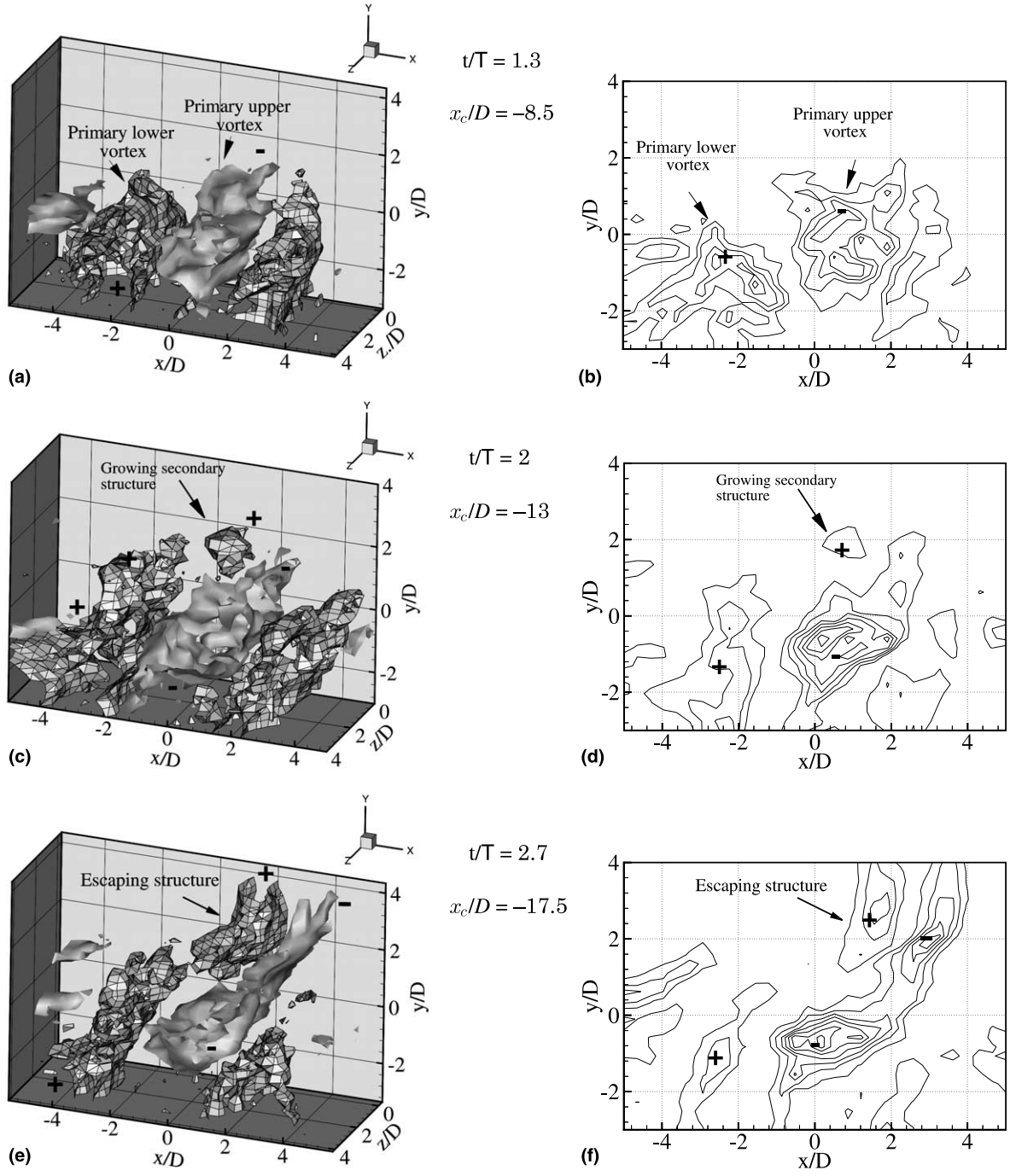

Fig. 9. Development of the spanwise vorticity distribution as derived from the 3D-PTV data for $Re_D = 75$ and $Ri_D = 1.3$. Left: iso-vorticity contour surfaces ($\omega_z = -0.25$ and $\omega_z = 0.15$) and right: iso-vorticity contours in a 2D-slice at $z/D = 1$ ($-1 < \omega_z < 1$ with step size 0.1). The position of the cylinder is denoted with x_c/D.

are not yet available, the present visualisation results show that the spanwise length-scale of these secondary structure is around 4D. This spanwise distribution coincides with the critical spanwise wave number of the low Reynolds number instability for a forced convection flow ($Ri_D = 0$) as observed by Williamson [2] and

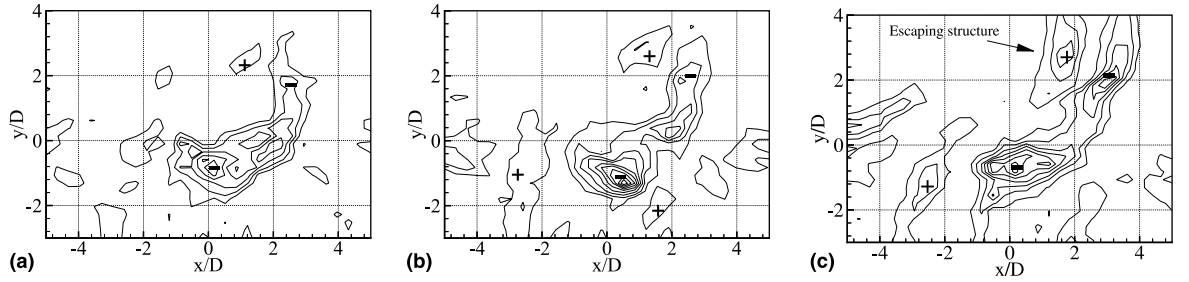

Fig. 10. Spanwise vorticity distribution as derived from the 3D-PTV data for $Re_D = 75$ and $Ri_D = 1.3$ at three cross-sections: (a) $z/D = 4$, (b) $z/D = 2$ and (c) $z/D = 1$ considered at time $t/\mathrm{T} \approx 2.7$. The cylinder is positioned in $x/D = -17.5$.

Barkley and Henderson [18]. Their investigations have shown that for $180 < Re_D < 259$ the flow is most sensitive for disturbances with a typical wavelength of 4D. Although for the Re_D considered in the present investigation the stability analysis of [18] predicts an unconditionally stable 2D flow field, it is remarkable to see that the spanwise length-scale of the secondary structures is about the same.

Acknowledgements

This work is part of the research programme of the Netherlands Foundation for Fundamental Research on Matters (FOM), which is financially supported by the Netherlands Organisation for Scientific Research (NWO). The authors would like to take the opportunity to thank the technical staff of the Energy Technology section for their support.

References

[1] M.M. Zdravkovich, Flow Around Circular Cylinders, Oxford University Press, Oxford, 1997 (Chapter 3).
[2] C.H.K. Williamson, Three-dimensional wake transition, J. Fluid Mech. 328 (1996) 345–407.
[3] O.M. Griffin, E.S. Ramberg, Vortex shedding from a cylinder vibrating in line with an incident uniform flow, J. Fluid Mech. 75 (1976) 257–271.
[4] G.H. Koopmann, The vortex wakes of vibrating cylinders at low Reynolds, J. Fluid Mech. 28 (1967) 501–512.
[5] M.E. Davies, A comparison of the wake structure of a stationary and oscillating bluff body, using a conditional averaging technique, J. Fluid Mech. 75 (1976) 209–231.
[6] K. Noto, R. Matsumoto, Numerical simulation on the development of the Karman vortex street due to the negatively buoyant force, in: Proc. 5th Conf. on Numerical Methods in Laminar Flow, Pineridge Press, Swansea, 1987, pp. 796–809.
[7] H.M. Badr, Laminar combined convection from a horizontal cylinder-parallel and contra flow regimes, Int. J. Heat Mass Transfer 27 (1984) 15–27.
[8] N. Michaux-Leblond, M. Bélorgey, Near-wake behavior of a heated circular cylinder: viscosity–buoyancy duality, Exp. Therm. Fluid Sci. 15 (1997) 91–100.
[9] R.N. Kieft, C.C.M. Rindt, A.A. van van Steenhoven, Destabilizing effect of heat on coherent structures, in: S. Banerjee, J.K. Keaton (Eds.), First Int. Symp. on Turbulence and Shear Flow, St-Barbara, USA, Begell House, New York, 1999, pp. 127–1032.
[10] R.N. Kieft, C.C.M. Rindt, A.A. van van Steenhoven, The influence of buoyancy on the behavior of the vortex structures in a cylinder wake, in: Presented at the 11th Int. Heat and Mass Transfer Conf., Kyongju, Korea, pages Paper no. 26 PM, EC(2), 1998.
[11] R.M. Kieft, C.C.M. Rindt, A.A. van van Steenhoven, The wake behaviour behind a heated horizontal cylinder, Exp. Therm. Fluid Sci. 19 (1999) 183–193.
[12] G.A.J. van der Plas, R.N. Kieft, C.C.M. Rindt, Application of a 2D high resolution particle veclocimetry method on mixed convection flows, in: Third Int. Workshop on PIV'99, USCA-University Press, 1999, pp. 177–182.
[13] K.R.A.M. Schreel, G.A.J. van der Plas, R.N. Kieft, Accuracy of a 3D particle tracking velocimetry method, in: 9th Int. Symp. on Flow Visualisation, 2000.
[14] Y. Maday, A.T. Patera, E.M. Ronquist, An operator–integration-factor splitting method for time-dependent problems: applications to compressible flow, J. Sci. Comput. 5 (1990) 263–291.
[15] L.J.P. Timmermans, P.D. Minev, F.N. van de Vosse, An approximate projection scheme for incompressible flow using spectral elements, Int. J. Numer. Meth. Fluids 22 (1996) 673–688.
[16] C. Cuvelier, A. Segal, A.A. van Steenhoven, Finite Element Methods and Navier Stokes Equations, Reidel, Dordrecht, 1986.
[17] C. Agui, J. Jimenez, On the performance of particle racking, J. Fluid Mech. 185 (1987) 447–468.
[18] D. Barkley, R.D. Henderson, Three-dimensional Floquet stability analysis of the wake of a circular cylinder, J. Fluid Mech. 322 (1996) 215–241.